Near-Field Scanning Optical Microscopy Enables Direct Observation of Moiré Effects at the Nanometer Scale
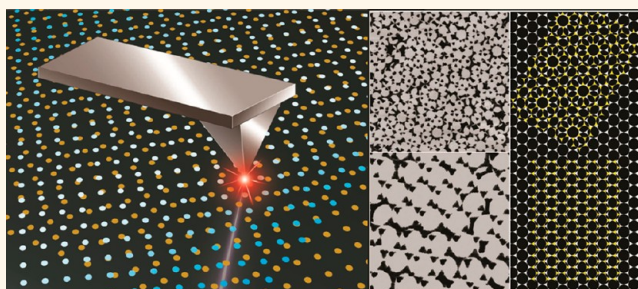
Wei-feng Lin, Jie-Ren Li, and Gang-yu Liu*

Department of Chemistry, University of California, Davis, California 95616, United States

The Moiré effect is a well-known optical phenomenon that occurs when two periodic or quasi-periodic patterns are superposed.[1] In the overlapped region, a new periodic structure with the superperiodicity appears, as captured by the far-field optical signal. The Moiré effect is very sensitive to small displacements or distortions of the basic patterns and their superposition status. Such sensitivity has attracted much attention to application of Moiré techniques in optical alignments,[2] metrology,[3,4] and strain analysis.[5,6] The concept and Moiré techniques are mostly limited to the micrometer region thus far, due to the diffraction limit of far-field optics.[7]

To overcome the diffraction limit and extend Moiré techniques to the nanometer scale, various approaches have been reported. Current methods in generating Moiré nanostructures include self-assembly,[8−11] nanoimprint lithography,[12,13] and crystallization.[14] In terms of surface characterization, scanning tunneling microscopy (STM) was utilized to investigate metal Moiré nanostructures extensively, from which superperiodicity can be observed due to the mismatch of lattice constants between the adlayer and the substrate.[15−20] In addition, atomic force microscopy (AFM) also characterized Moiré patterns at the nanometer scale for a broad range of materials.[8,13,21−23] Those prior investigations demonstrated the formation of Moiré patterns at nanoscale levels. The resulting new periodic structures were characterized by non-optical techniques such as STM and AFM. Very recently, optical characterization of the Moiré effect at the nanoscale became successful after a special enhancement technique: inserting a silver slab between two subwavelength gratings and taking advantage of the surface

plasmon polariton excitation by the silver slab.[7] These recent developments naturally lead to a next challenge: whether the Moiré effect at nanoscale can be probed directly without modifying the Moiré pattern or artificial enhancement.

This work presents our approach to this inquiry using near-field scanning optical microscopy (NSOM). The near-field imaging concept is based on Synge's idea that a light source with size smaller than the wavelength

ABSTRACT

This work reports probing the Moiré effect directly at the nanometer scale *via* near-field scanning optical microscopy (NSOM). Periodic metal nanostructures of Au and Cu have been produced sequentially using particle lithography, and the overlapped regions serve as Moiré patterns at nanometer scale. The Moiré effect in these regions can be directly visualized from NSOM images, from which periodicity and structural details are accurately determined. In addition, the near-field Moiré effect was found to be very sensitive to structural changes, such as lateral displacement and/or rotations of the two basic arrays with respect to each other. Further, nanostructures of Cu exhibited higher photon transmission than Au from NSOM images. Collectively, NSOM enables direct visualization of the Moiré effect at nanoscale levels, from optical read out, and without enhancements or modification of the structures. The results demonstrate the feasibility to extend applications of the Moiré effect-based techniques to nanometer levels.

KEYWORDS: Moiré effect · Moiré pattern · particle lithography · near-field scanning optical microscopy
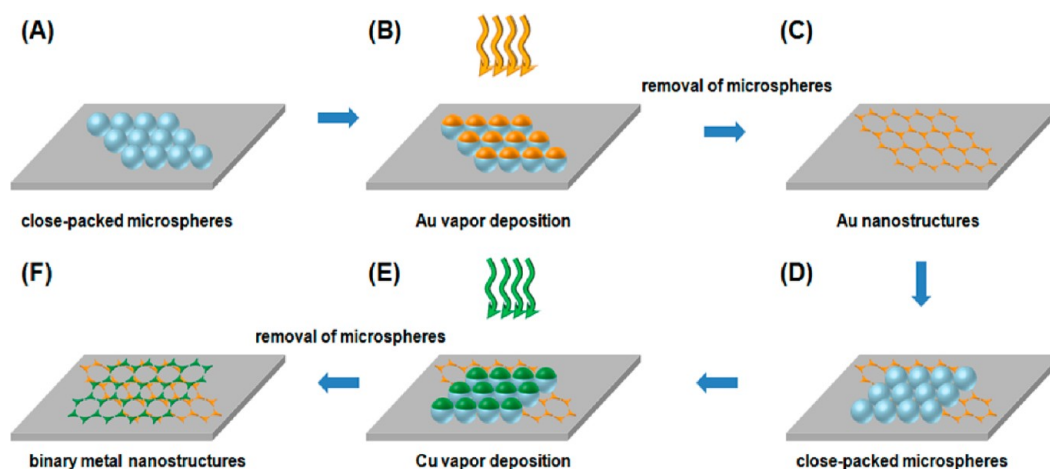
Figure 1. Key steps for fabricating arrays of superposed metal nanostructures *via* sequential particle lithography. (A) Monolayer of silica microspheres are formed *via* drop-dry method on a glass substrate. (B) Au is deposited *via* vapor deposition on glass through the silica particle mask. (C) Microsphere template is removed by sonication. (D) New monolayer of close-packed microspheres is deposited on the glass region containing Au nanostructures. (E) Cu is deposited *via* vapor deposition onto the substrate through the second mask. (F) Second silica template is removed *via* sonication.

can scan a sample point-by-point, sequentially probing its optical property.[24] NSOM is a powerful imaging tool since it provides spectroscopy information at nanoscale levels in correlation with morphological details.[25−31] The intrinsic advantages of NSOM provide great promise. However, conventional aperture NSOM has great difficulty detecting the Moiré effect due to low photon throughput, difficulties in operation, and insufficient spatial resolution. This work utilizes a home-built apertureless NSOM for the investigation of the Moiré effect.[32,33] In this design, NSOM light source was produced by excitation of commercial silicon nitride (Si_3N_4) AFM probes with an ultraviolet laser (*e.g.*, 405 nm). Such a light source has the intrinsic advantages of stability, durability, and high emission intensity. In addition, utilizing bright photoluminescent (PL) probes simplifies the separation and detection of near-field signals because the PL exhibits different wavelength from the far-field excitation beam. Arrays of two superimposed metal nanostructures were fabricated sequentially by using particle lithography.[34] Near-field Moiré effect was demonstrated and found to be very sensitive to small lateral displacement and/or rotation between the two basic arrays. In addition, our NSOM contrast could distinguish various metals in the composites. The results from this investigation bring us one step closer to realize the Moiré effect's application at the nanometer scale.

RESULTS AND DISCUSSION

Fabrication of Two Superposed Arrays of Metal Nanostructures by Sequential Particle Lithography. The key steps for producing superposed arrays of metal nanostructures are illustrated in Figure 1. Details about the fabrication process can be found in the Materials and Methods section. Briefly here, the sample was prepared by overlaying periodic Cu nanostructures on Au nanostructures.

To prepare an array of periodic Au nanostructures, a monolayer of close-packed silica beads was first formed by dropping 35 μL of silica sphere solution on a glass surface.[35−38] These silica spheres serve as a mask for subsequent Au vapor deposition *via* thermal evaporation.[34] The mask was removed by sonication in ethanol. The diameter of the silica beads determines the periodicity of the array, and the voids dictate the size and geometry of the metal islands. The resulting Au islands are typically triangular-shaped, as Au vapor passed through the triple hollow voids and deposited on glass.

After Au nanostructures, periodic Cu nanostructures were produced and overlaid onto the Au region. The procedure began with rinsing and sonicating the sample to remove any residues from the first particle masks and metal deposition. The second mask of silica particles was then produced prior to Cu deposition. The final structure was exposed to hydrogen flame after mask removal.

NSOM Enables Direct Observation of the Moiré Effect at the Nanometer Scale. To characterize the produced nanostructures, a home-constructed multifunctional microscope combining atomic force microscope (AFM), near-field scanning optical microscope (NSOM), and far-field optical microscope was used.[32,33,38] The detailed setup and operation has been reported previously. The near-field scanning optical microscopy used for this work follows an apertureless configuration.[30,31] Figure 2A shows the schematic of the optical path. Upon excitation by, for example, a focused 405 nm beam, Si_3N_4 probes emit PL, as shown in Figure 2B. A typical spectrum corresponding to the true color photograph is shown in Figure 2C, a broad peak maximized at 605 nm. Figure 2D reveals the exponential decay of PL signal when the tip is within 150 nm of contact. The exponential relationship between the PL
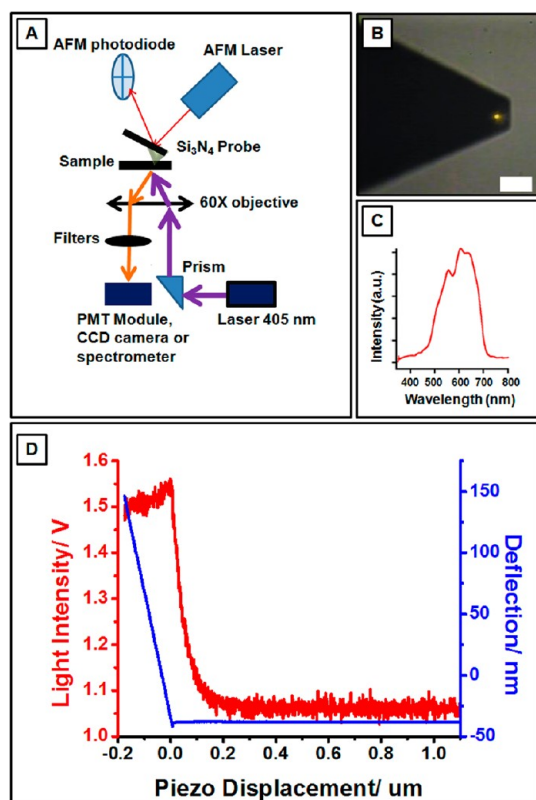
Figure 2. (A) Schematic of the combined atomic force microscope, near-field scanning optical microscope, and far-field optical microscope. (B) Photograph of the photoluminescence of a Si_3N_4 probe upon excitation (λ = 405 nm). The scale bar is 25 μm. (C) Photoluminescent spectrum of (B). (D) Photoluminescent signal (red) and cantilever deflection signal (blue) as a function of the tip–surface separation.

intensity and tip–surface separation distance indicates the evanescent or near-field nature of the optical signal.[29,30] The decay length of the optical near-field is 55 nm, as per least squares fitting.

Figure 3 reveals the NSOM and simultaneous AFM images of individual and overlapped Au and Cu arrays. Figure 3A,B shows NSOM and simultaneous AFM topographic images of an array of Au nanostructures. The morphology exhibits the characteristic hexagons with Au nanotriangular islands at each corner. The side length of individual Au islands measures 306 $\pm$ 10 nm. The heights of the Au islands are 45 $\pm$ 2 nm. This is consistent with previous reports of Au nanostructures prepared by particle lithography.[34,39] The unit cell for this periodic structure is indicated by the orange oblique in Figure 3A,B. The lattice constants can be measured directly from Figure 3A,B or via fast Fourier transform (FFT), shown as the insets, where $a_{Au} = b_{Au} = 747 \pm 3$ nm, $\alpha_{Au} = 120 \pm 1°$.

Figure 3C,D shows NSOM and simultaneous AFM topographic images of Cu array acquired from a non-overlapping region. Similar to the Au array, Cu layers exhibit the hexagonal features with triangular islands at each corner. The side length of individual Cu islands
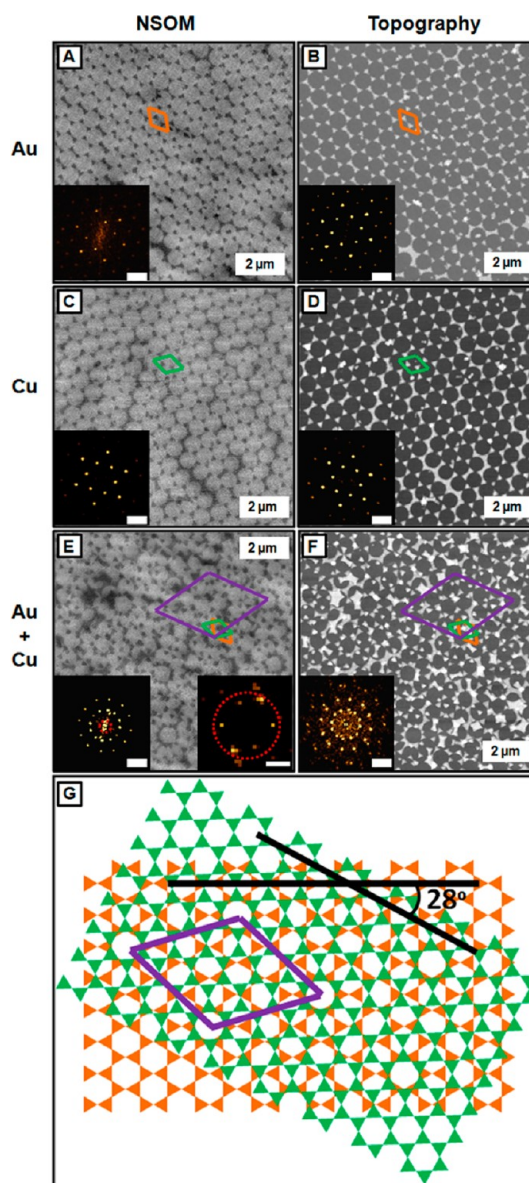

Figure 3. Moiré effect at nanoscale is demonstrated *via* NSOM. (A) A 10 $\times$ 10 μm^2 NSOM image of the Au periodic nanostructures, with FFT as inset. (B) Simultaneously acquired AFM topographic image of (A) with its FFT inserted. (C) A 10 $\times$ 10 μm^2 NSOM image of the Cu periodic nanostructures, with FFT as inset. (D) Simultaneously acquired AFM topographic image of (C) with its FFT inserted. (E) A 10 $\times$ 10 μm^2 NSOM image of the arrays of superposed metal nanostructures. Left inset is the corresponding FFT analysis for the NSOM image. Right inset highlights the signal corresponding to the superlattice in reciprocal space, with scale bar equal to 0.4 μm^{-1}. (F) Simultaneously acquired AFM topographic image of (E) with its FFT inserted. The scale bars for all FFT images are 2 μm^{-1} unless specified above. (G) Structural model extracted from the images above. Moiré pattern is generated by overlapping the periodic Cu lattice on the Au array with the same origin, then rotating the Cu array clockwise by 28°. Superperiodicity of the Moiré pattern is indicated as the purple unit cell.

measures 304 $\pm$ 11 nm. The height of the Cu islands is 46 $\pm$ 3 nm. The unit cell of the Cu lattice is labeled green in Figure 3C,D. The FFT analysis insets reveal the
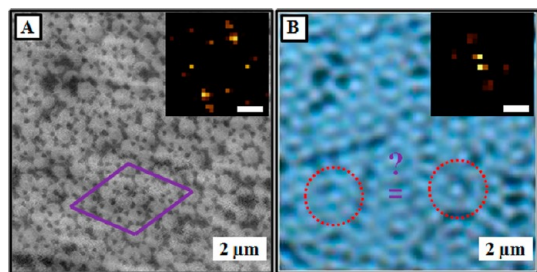
Figure 4. Direct comparison of NSOM and far-field images of the same region. (A) A 10 × 10 μm^2 NSOM image of the Moiré nanopattern. The FFT (inserted) as discussed in Figure 3E clearly reveals the periodicity of the superlattice. (B) Conventional optical image of the same region, where much blurry contrast is shown without detectable superlattice in the FFT (inset). The scale bars in the FFT image are 0.4 μm^{-1}.

lattice constant of Cu nanostructures to be $a_{Cu} = b_{Cu} = 742 \pm 4$ nm, with $\alpha_{Cu} = 120 \pm 1°$.

NSOM and AFM images of the overlaying region are shown in Figure 3E,F, respectively. In contrast to hexagonal features, the NSOM image in Figure 3E clearly reveals a more complex morphology and a superperiodicity of rosette-like patterns. This new lattice is consistent with a superstructure from the two basic fringes of the Au and Cu arrays. The unit cell of the new fringe is indicated by the purple oblique in images 3E and 3F. The lattice constants measure $a_s = b_s = 2.66 \pm 0.03 \mu m$ and $\alpha_s = 120 \pm 2°$. The FFT analysis is shown in the left inset of Figure 3E, where 12 bright spots near the origin are visible, six from the Au lattice, and the other six from the Cu lattice. The angle θ between the two basic Au and Cu lattices, measured from FFT analysis in Figure 3E, is $28 \pm 1°$. The periodicity of the superlattice can be extracted from the corresponding FFT (inset on the right of Figure 3E). Analogous to Moiré demonstration in micrometer scale, the appearance of the rosette-like structure in NSOM is rationalized in Figure 3G, that is, overlapping the periodic Cu lattice on the Au array with the same origin, then rotating the Cu array clockwise by 28°. While a Moiré pattern at the nanoscale has been demonstrated by AFM in the past, Figure 3E represents the first and direct observation of the Moiré effect at nanometer scale using true optical signal, to the best of our knowledge. While AFM topographs allow visualizing the lateral geometry and height of nanoislands, NSOM contrasts carry the spectroscopy information. The difference in contrast can be seen by the difference in FFT images, in which the brightness of FFT spots corresponds to NSOM images carrying the information of optical intensity. The sensitivity of NSOM to materials will be further discussed in a later section.

The enabling aspect of NSOM is further demonstrated in Figure 4, where a close comparison between near-field image and far-field image was made in the same region. Figure 4A is a 10 × 10 μm^2 NSOM image, from which the superlattice and rosette-like patterns

are clearly visible. In addition, individual Au and Cu triangular nanoislands are also clearly resolved. The inset in Figure 4A shows the superlattice signals in the FFT image. Using a bright-field 60× objective and immersion oil (Olympus), a high-resolution far-field image was captured, as shown in Figure 4B. While there are some rosette-like features, no periodicity could be extracted as each rosette appears to be different from the other. In the corresponding FFT (4B inset), superlattice points cannot be generated. The inability to capture the Moiré effect at the nanoscale by conventional optical microscopy is consistent with prior knowledge of diffraction limit.[25] In this Moiré pattern, the sizes of the metal nanoislands are 306 nm, at which scale visible wavelength at far-field is difficult to resolve.

Near-field Moiré effect was found to be very sensitive to small lateral displacements and/or rotational angles between the same two basic arrays of nanostructures. Figure 5 compares two Moiré patterns originated from the same two basic lattices. Figure 5A,B represents the Moiré pattern discussed in Figure 3E. It was generated by overlaying the Cu array on the top of the Au array with the same origin, and then rotating the Cu array clockwise by 28°, as described in a previous section. A different Moiré pattern is revealed in Figure 5D,E, exhibiting zig-zagged rod-like features, in contrast to the rosette-like pattern shown in 5A. The unit cell of the superlattices is labeled in purple. The lattice constants measured $a_s = b_s = 743 \pm 12$ nm and $\alpha_s = 120 \pm 2°$. Note that these lattice parameters are the same as the two basic lattices of Au and Cu arrays. In addition, individual Au and Cu triangular islands are clearly resolved by NSOM. The inset FFT analysis shows only six-fold symmetric signals, which represent the overlapping of the two basic lattices. The corresponding Moiré pattern extracted from the real and reciprocal space images shown in Figure 5D is shown in 5F: overlaying Cu array with Au array, and then moving the Cu array to the right by 162 nm, without rotation. Although Moiré patterns in Figure 5A,D are from the same Au and Cu lattices, the resulting NSOM contrast significantly differs due to the difference in the overlapping.

NSOM Enables Distinguishing Chemical Components within the Moiré Patterns. Using the overlapped arrays of metal nanostructures as a testing platform, the capability of NSOM to distinguish materials is explored. Figure 6 shows two different sets of experiments. Pattern 1 (top panel) was prepared by overlaying periodic Au onto periodic Cu arrays. The Cu array with periodicity of 5.0 μm was produced on the substrate, and then Au nanoislands with a periodicity of 1.57 μm were deposited. Figure 6A is the AFM topographic image revealing the overlapping region. To facilitate the comparison, we purposely produced the two materials with different sizes but the same height. The larger triangles are
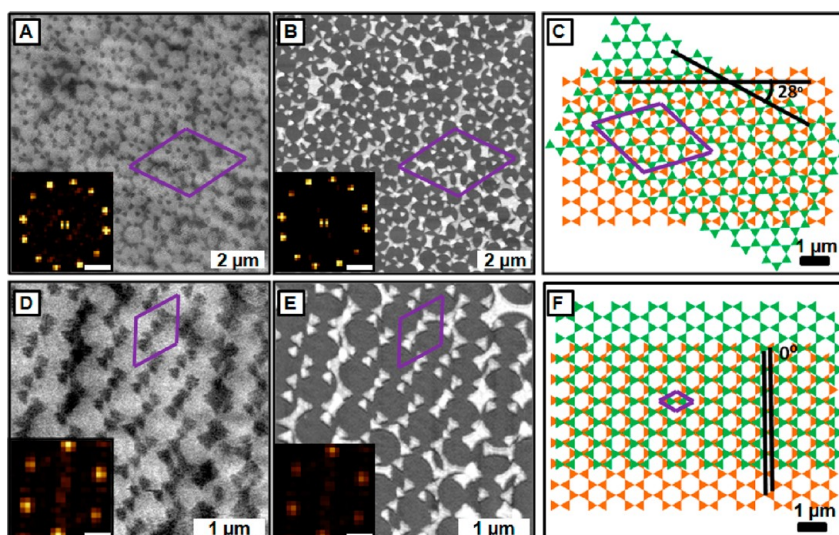
Figure 5. High sensitivity of near-field Moiré effect to structural changes at nanoscale. (A) A $10 \times 10 \, \mu m^2$ NSOM image of the arrays of superposed metal nanostructures. (B) Simultaneously acquired AFM topographic image of (A) with its FFT inserted. (C) Structural model extracted from (A). Moiré pattern is generated by overlapping the periodic Cu lattice on the Au array with the same origin, then rotating the Cu array clockwise by 28°. Superperiodicity of the Moiré pattern is indicated as the purple unit cell. (D) A $4.5 \times 4.5 \, \mu m^2$ NSOM image of the arrays of superposed metal nanostructures. (E) Simultaneously acquired AFM topographic image of (D) with its FFT inserted. (F) Structural model extracted from (D). Moiré pattern is generated by overlaying Cu array with Au array, and then moving the Cu array to the right by 162 nm, without rotation. The scale bars in FFT image are $1 \, \mu m^{-1}$.
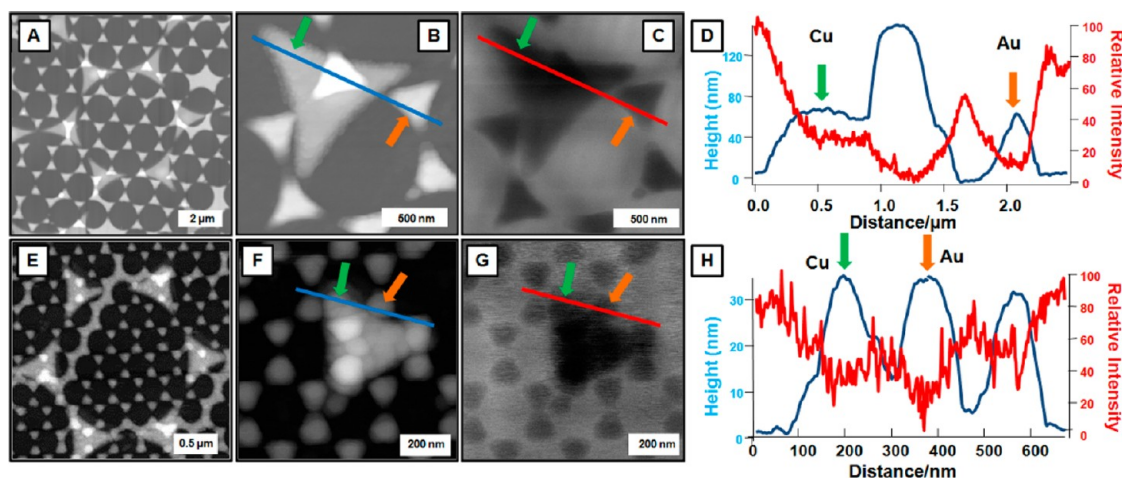

Figure 6. A micro and a nano Moiré pattern, as imaged by NSOM. (A) A $11 \times 11 \, \mu m^2$ topographic image of a micro Moiré pattern: Au arrays ($a_{Au} = b_{Au} = 1.57 \, \mu m$, $\alpha_{Au} = 120 \pm 2°$) on the top of Cu arrays ($a_{cu} = b_{cu} = 5.0 \, \mu m$, $\alpha_{cu} = 120 \pm 2°$). (B) Zooming into (A) to reveal the structural details. (C) Simultaneously acquired NSOM image corresponding to (B). (D) Combined cursor profiles for lines defined in (B) and (C). (E) A $2.5 \times 2.5 \, \mu m^2$ topographic image of a nano Moiré pattern: Au arrays ($a_{Au} = b_{Au} = 300 \, nm$, $\alpha_{Au} = 120 \pm 2°$) on the top of Cu arrays ($a_{cu} = b_{cu} = 1.57 \, \mu m$, $\alpha_{cu} = 120 \pm 2°$). (F) Zooming into (E) to reveal the structural details. (G) Simultaneously acquired NSOM image corresponding to (F). (H) Combined cursor profiles for lines defined in (F) and (G).

Cu islands. The side length of the Cu islands measures 2350 ± 50 nm with the height of 73 ± 5 nm. The smaller triangles are Au islands with 740 ± 50 nm side length and 75 ± 4 nm thickness. Figure 6B,C shows the simultaneous AFM and NSOM images upon zooming into 6A, where the structural details of a concave Cu triangle and a Au hexagon are revealed. Figure 6D is the combined cursor profiles as indicated in 6B and 6C. For local regions of Au and Cu islands with the same thickness, Cu islands (green arrow) have higher optical

transparencies than Au islands (orange arrow) in the near-field contrast.

The same trend exists at much reduced sizes such as in pattern 2 imaged in Figure 6E. This Moiré pattern was prepared by overlaying Au onto Cu arrays. First, Cu arrays with a periodicity of 1.57 μm were patterned on substrate and Au arrays with a periodicity of 300 nm atop. Figure 6E is the AFM topographic image of pattern 2. In this image, the larger metal islands are Cu islands; the side length is 630 ± 23 nm and height
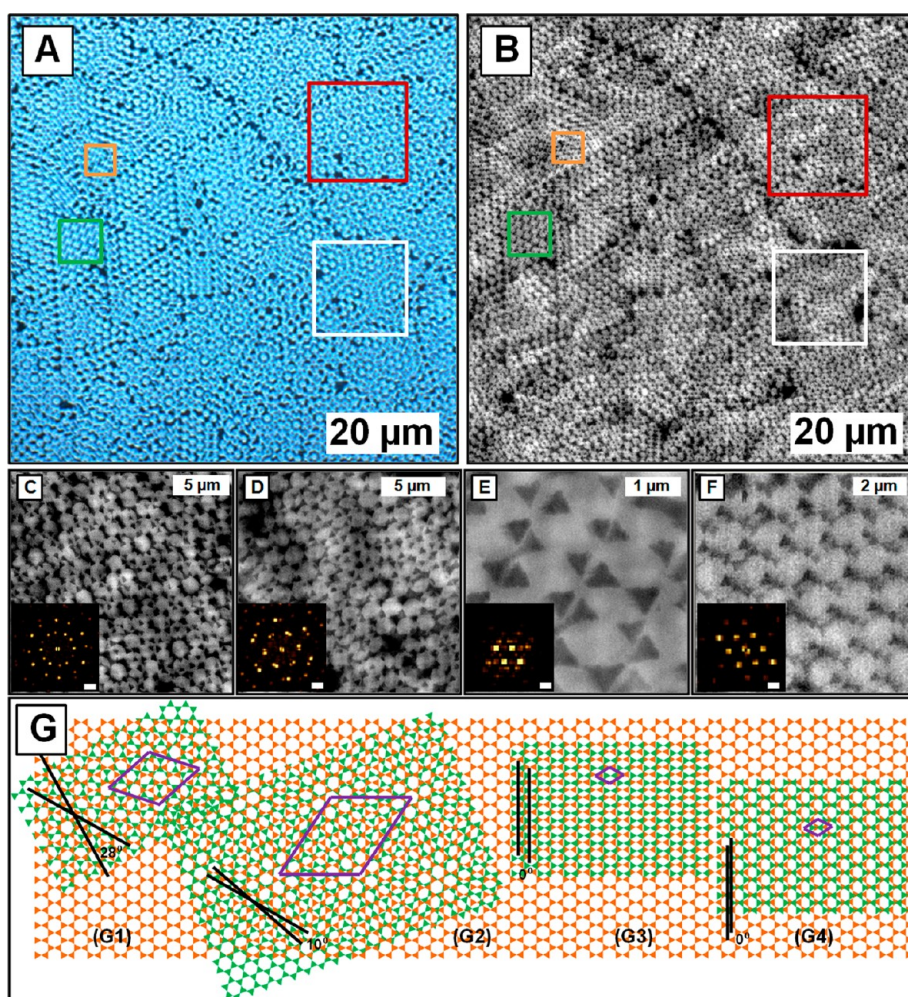
Figure 7. Particle lithography enables production of polymorphic Moiré patterns. (A) An 80 × 80 μm^2 optical image acquired using a 60× oil immersion objective over Cu arrays (periodicity = 1.57 μm) on the top of Au arrays (periodicity = 1.57 μm). (B) Corresponding NSOM image acquired in the same region as in (A). (C) A 25 × 25 μm^2 NSOM image from zooming into the region in (A) (red box). (D) A 16 × 16 μm^2 NSOM image from zooming into the region in (A) (white box). (E) A 4 × 4 μm^2 NSOM image from zooming into the region in (A) (orange box). (F) An 8 × 8 μm^2 NSOM image from zooming into the region in (A) (green box). The scale bars for all FFT images are 0.6 μm^{-1}. (G) Structural models of the 4 Moiré patterns in (C−F).

measurements of 33 ± 2 nm. The smaller metal islands are Au islands; the side length of the Au islands is 125 ± 11 nm, with height measurements of 34 ± 2 nm. Figure 6F,G represents the AFM topographic and NSOM images, respectively, upon zooming into the region within Figure 6E. Both metal arrays were clearly resolved in the near-field image. Figure 6H is the combined cursor profiles as indicated in Figure 6F,G. With the same feature height, Cu islands (green arrow) have higher optical transparencies than Au islands (orange arrow). The observation that Au exhibits less optical transparency than Cu can be rationalized by the following. Cu metal is prone to oxidation upon exposure to ambient atmosphere at room temperature.[40] The thin oxide layers (nanometers) are dominated by Cu_2O mixed with CuO.[40,41] Prior work indicated that Au and Cu nanoislands exhibit similar optical properties; however, formation of thin oxide crust on Cu islands red shifts and broadens the plasmonic extinction and,

therefore, resulted in higher transparency in the visible range.[41] The near-field contrasts in our setup are, therefore, consistent with the reported plasmonic property of Au and Cu islands. The enabling aspect of NSOM in probing optical properties with high spatial precision, shown in this work, as well as other NSOM investigations,[42−47] shall bring us another step closer to spectral imaging at molecular and atomic resolution.

Particle Lithography Enables Production of Polymorphic Moiré Patterns. By controlling experimental conditions in particle lithography, such as solvent evaporation rate, we could attain a certain degree of control over the 2D single crystallinity of the close-packed silica particles.[35] Analogous to crystal growth, slow rate tends to produce larger domains of close-packed silica particles. At a fast rate, polycrystallinity occurs, which manifested into polymorphic Moiré patterns in the overlapping regions.[48] Figure 7A,B shows the far-field and near-field optical images of the bimetallic arrays in

the same $80 \times 80\ \mu m^2$ region. The structures were prepared by overlaying Cu arrays onto Au arrays, with periodicity = 1.57 μm. In Figure 7A, at least four types of Moiré patterns are clearly observed, as highlighted in red, green, purple, and blue squares, respectively. Figure 7B is the NSOM image taken in the same region as in Figure 7A, from which Moiré patterns are more clearly distinguished due to its higher resolution.

When the four types of patterns identified in Figure 7B were imaged by zooming-in, their Moire effects were more clearly visualized, in Figure 7C—F. Figure 7C reveals a superperiodicity with a rosette-like morphology. The lattice constants of the superlattice are $a_s = b_s = 5.64 \pm 0.04\ \mu$m, with $\alpha_s = 120 \pm 2°$. It was generated by overlapping the periodic Cu lattice on the Au array with the same origin, then rotating the Cu array clockwise by 28°, as illustrated in Figure 7G (G1). The pattern shown in Figure 7D exhibits domains of honeycomb clusters. The lattice constants of the superlattice are $a_s = 9.55 \pm 0.11\ \mu$m, $b_s = 8.32 \pm 0.08\ \mu$m, and $\alpha_s = 110 \pm 2°$. It was generated by overlapping the periodic Cu lattice on the Au array with the same origin, then rotating the Cu array clockwise by 10°, as illustrated in Figure 7G (G2). Figure 7E demonstrates a Moiré pattern composed of parallel lines of triangle pairs. The superlattice is overlapping with the two basic lattices, with lattice constants measured as $a_s = b_s = 1.57 \pm 0.2\ \mu$m and $\alpha_s = 120 \pm 2°$. It was produced by overlaying Cu array on Au array, then moving the Cu array toward the right by 800 nm, without rotation, as illustrated in Figure 7G (G3). Moiré pattern in Figure 7F consists of zig-zagged rods. The superlattice is overlapping with the two basic lattices, with lattice constants measured as $a_s = b_s = 1.57 \pm 0.2\ \mu$m and $\alpha_s = 120 \pm 2°$. It is the result of overlaying a Cu array on a Au array, then moving the Cu array toward the right by 350 nm, without rotation, as illustrated in Figure 7G (G4).

The coexistence of multiple types of Moiré patterns in one sample and within the small region is due to the polycrystallinity of silica sphere arrays formed during the drying process. The polycrystallinity in templates transferred to the Au and Cu arrays and as such polymorph occurs. Polycrystallinity is typically considered a disadvantage if the goal were to produce metal nanostructure arrays with high-throughput. One could reduce this effect using similar approaches by growing large crystals, such as by slowing down the vaporization rate and/or increasing temperature. In the case of Figure 7, we purposely fabricated the polymorph to demonstrate the sensitivity of the Moiré effect to crystalline defects, overlaying status, within one image frame.

CONCLUSION

NSOM enables a direct optical probe of the Moiré effect at nanoscale levels without additional surface modification or enhancement. In the Moiré patterns of metal nanostructures produced using particle lithography, the near-field Moiré effect is found to be very sensitive to structural changes such as nanoscale lateral displacements and/or rotations between the two basic arrays. The NSOM enables spectroscopic information to be acquired while topographic images are taken; for example, Au nanostructures transmit less photons than Cu in the visible region. The difference in plasmonic properties manifests into clear contrast and high resolution in near-field images, from which the periodicities of basic and superlattice are determined. These enabling aspects bring us one step closer to extend the applications of the current Moiré effect-based techniques to the nanometer scale. The new apertureless configuration enables spectroscopy information to be acquired at nanometer scale, which greatly enhances the structural characterization capabilities of scanning probe microscopy. Work is in progress to improve sensitivity and spatial resolution and to utilize spectroscopic information for nanomaterial characterization.

MATERIALS AND METHODS

Materials. Glass coverslips (No.1) were purchased from Corning (Corning, NY) with lateral dimensions of 18 mm × 18 mm and thicknesses of 0.18 mm. Au slugs (99.999%) and Cu slugs (99.999%) were from Alfa Aesar (Ward Hill, MA). Ethanol (EtOH, 99.99%) was purchased from Gold Shield Chemical Co. (Hayward, CA). Sulfuric acid (95.0%), hydrogen peroxide (30% aqueous solution), ammonium hydroxide (30% aqueous solution), tetrahydrofuran (THF, 99.5%), and toluene (HPLC grade) were purchased from EMD Chemicals (Gibbstown, NJ) and used as received. Water (≥ 18.2 M$\Omega\cdot$cm) was generated from a Milli-Q system (Q-GARD 2, Millipore, Billerica, MA) and used for dilution and washing. Nitrogen gas (99.999%) and hydrogen gas (99.95%) were purchased from Praxair, Inc. (Danbury, CT). Polystyrene latex spheres with diameters of $5.0 \pm 0.3\ \mu$m and 296 ± 6 nm and silica microspheres with diameters of 0.73 ± 0.02 and $1.57 \pm 0.02\ \mu$m were purchased from Thermo Scientific (Waltham, MA). The spheres were suspended in their original concentration of 2% (w/v, aqueous) until usage.

Preparation of Arrays of Overlapped Metal Nanostructures. Glass coverslips were cleaned following reported protocols.[38,49,50] In brief, they were cleaned by immersion in piranha solution for 1 h and subsequently in a basic bath for 1 h. Substrates were then rinsed with copious quantities of ultrapure water and dried in nitrogen gas.

The overlapped arrays of metal nanostructures were fabricated on glass substrates. They were prepared by sequential deposition of metal vapors through two different particle templates. The Moiré nanopatterns are composed of Au and Cu arrays with a periodicity of 0.73 μm. Monolayers of a silica sphere ($D = 0.73\ \mu$m) template for Au vapor deposition were prepared following the reported protocols.[34,38,49−52] A 45 nm Au thin film was deposited onto the sphere template in a high-vacuum evaporator (model DV502-A, Denton Vacuum Inc., Moorestown, NJ) at 10^{-7} Torr at room temperature. The evaporation rate was monitored by a quartz crystal monitor (Inficon Inc., East Syracuse, NY) and controlled between 0.10 and 0.15 nm/s. After Au deposition, the sphere template was

removed by sonication in EtOH for 3 s. The substrates were subsequently rinsed with water and exposed to hydrogen flame to remove any organic contaminant. The choice of solvent for the particles is also important since the surface is uneven. EtOH was found to be the optimal solvent, by which the homogeneity of the silica sphere thin film can be improved. A suspension of silica spheres ($D = 0.73\ \mu m$) in EtOH solution was deposited onto the patterned Au arrays and allowed to dry. The dried particle mask served as a material guide for the subsequent deposition of a 45 nm Cu thin film. Then, the silica sphere masks were removed by sonication in EtOH for 3 s. The substrates were rinsed with EtOH and exposed to hydrogen flame to remove any contaminant. The Moiré micropattern is composed of Au and Cu arrays with a periodicity of 1.57 μm. It was prepared by similar procedures as described above.

Home-Built Combined Atomic Force, Near-Field Scanning Optical, and Far-Field Optical Microscopy. The setup has been reported previously by our team. Briefly, an AFM scanner (MFP-3D, Asylum Research Corp., Santa Barbara, CA) was mounted on an inverted optical microscope (IX-50, Olympus America, Center Valley, PA) modified in-house. The excitation laser (405 nm, 4 mW, World Star Tech., Toronto, Canada) was focused onto a Si_3N_4 AFM tip through a $60\times$ bright-field objective (NA = 1.45, Olympus America, Center Valley, PA) using immersion oil ($n = 1.52$, type HF, Cargille Laboratories, Cedar Grove, NJ). The PL generated by the AFM probe was collected by the same objective and passed through a series of filters to remove excitation and AFM photons: a long-pass filter (HQ430LP, Chroma Technology Corp., Bellows Falls, VT) to filter the 405 nm photons; a short-pass filter (SP01-785RU-25, Semrock Inc., Rochester, NY) to remove the 850 nm photons from AFM. PL signals were collected by a photomultiplier tube (PMT, H5784-01, Hitachi, Schaumburg, IL), with a gain of 2×10^5 at control voltage of 0.80 V. The PMT signals were recorded simultaneously with AFM topography and deflection. The PL spectrum was attained by introducing a spectrometer (USB2000, Ocean Optics, Dunedin, FL) in the light path before PMT. A CCD camera (Regtiga-2000R, QImaging, Surrey, Canada) was used for true color far-field imaging.

All of the AFM and NSOM images were acquired under contact mode with imaging forces of 15−25 nN. Si_3N_4 cantilevers with a spring constant of 0.1 N/m were purchased from Veeco Probes (NP, Santa Barbara, CA) and Nanoink (DNP Probes, Skokie, IL). The AFM and NSOM images were acquired and analyzed using Asylum MFP3D software developed on the Igor Pro 6.12 platform. The PL intensity decay length fitting was analyzed by OriginPro 8.5.1.

Conflict of Interest: The authors declare no competing financial interest.

REFERENCES AND NOTES

1. Amidror, I.; Hersch, R. D. Fourier-Based Analysis and Synthesis of Moirés in the Superposition of Geometrically Transformed Periodic Structures. *J. Opt. Soc. Am. A* **1998**, *15*, 1100–1113.
2. Yan, W.; Yang, Y.; Chen, W.; Hu, S.; Zhou, S. Moiré-Based Focusing and Leveling Scheme for Optical Projection Lithography. *Appl. Opt.* **2010**, *49*, 5959–5963.
3. Chen, B. C.; Basaran, C. Statistical Phase-Shifting Step Estimation Algorithm Based on the Continuous Wavelet Transform for High-Resolution Interferometry Metrology. *Appl. Opt.* **2011**, *50*, 586–593.
4. Shao, J.; Ding, Y.; Tian, H.; Li, X.; Li, X.; Liu, H. Digital Moiré Fringe Measurement Method for Alignment in Imprint Lithography. *Opt. Laser Technol.* **2012**, *44*, 446–451.
5. Yang, W.; Huang, L.; Zhang, R.; Wang, M.; Li, Z.; Jia, Y.; Lei, R.; Sheng, X. Electron Microscopy Studies of the Age-Hardening Behaviors in 6005A Alloy and Microstructural Characterizations of Precipitates. *J. Alloys Compd.* **2012**, *514*, 220–233.
6. Zander, M.; Nishinaga, J.; Iga, K.; Horikoshi, Y. Structural Properties of InAs-Based Nanostructures Grown on GaAs-(001) and GaAs(111)A by Area Selective Epitaxy. *Phys. Status Solidi C* **2012**, *9*, 218–221.
7. Liu, Z. W.; Durant, S.; Lee, H.; Xiong, Y.; Pikus, Y.; Sun, C.; Zhang, X. Near-Field Moiré Effect Mediated by Surface Plasmon Polariton Excitation. *Opt. Lett.* **2007**, *32*, 629–631.
8. He, Y.; Ko, S. H.; Tian, Y.; Ribbe, A. E.; Mao, C. D. Complexity Emerges from Lattice Overlapping: Implications for Nanopatterning. *Small* **2008**, *4*, 1329–1331.
9. Koyfman, A. Y.; Magonov, S. N.; Reich, N. O. Self-Assembly of DNA Arrays into Multilayer Stacks. *Langmuir* **2009**, *25*, 1091–1096.
10. Luchnikov, V.; Kondyurin, A.; Formanek, P.; Lichte, H.; Stamm, M. Moiré Patterns in Superimposed Nanoporous Thin Films Derived from Block-Copolymer Assemblies. *Nano Lett.* **2007**, *7*, 3628–3632.
11. Park, S.; Wang, J. Y.; Kim, B.; Xu, J.; Russell, T. P. A Simple Route to Highly Oriented and Ordered Nanoporous Block Copolymer Templates. *ACS Nano* **2008**, *2*, 766–772.
12. Choi, J. S.; Wehrspohn, R. B.; Gosele, U. Moiré Pattern Formation on Porous Alumina Arrays Using Nanoimprint Lithography. *Adv. Mater.* **2003**, *15*, 1531–1534.
13. Li, M. T.; Wang, J. A.; Zhuang, L.; Chou, S. Y. Fabrication of Circular Optical Structures with a 20 nm Minimum Feature Size Using Nanoimprint Lithography. *Appl. Phys. Lett.* **2000**, *76*, 673–675.
14. Reinmuller, A.; Schope, H. J.; Palberg, T. Transient Moiré Rotation Patterns in Thin Colloidal Crystals. *Soft Matter* **2010**, *6*, 5312–5315.
15. Fujita, D. Nanoscale Synthesis and Characterization of Graphene-Based Objects. *Sci. Technol. Adv. Mater.* **2011**, *12*.
16. Kobayashi, K. Mechanism of Subsurface Imaging in Scanning Tunneling Microscopy. *Ultramicroscopy* **1998**, *73*, 163–168.
17. Nie, S.; Bartelt, N. C.; Wofford, J. M.; Dubon, O. D.; McCarty, K. F.; Thurmer, K. Scanning Tunneling Microscopy Study of Graphene on Au(111): Growth Mechanisms and Substrate Interactions. *Phys. Rev. B* **2012**, *85*.
18. Pan, Y.; Shi, D. X.; Gao, H. J. Formation of Graphene on Ru(0001) Surface. *Chin. Phys.* **2007**, *16*, 3151–3153.
19. Qin, Z. H.; Liu, C. D.; Chen, J.; Guo, Q. M.; Yu, Y. H.; Cao, G. Y. Molecular Orientation and Lattice Ordering of C-60 Molecules on the Polar FeO/Pt(111) Surface. *J. Chem. Phys.* **2012**, *136*.
20. Vasiljevic, N.; Dimitrov, N.; Sieradzki, K. Pattern Organization on Cu(111) in Perchlorate Solutions. *J. Electroanal. Chem.* **2006**, *595*, 60–70.
21. Nony, L.; Bocquet, F.; Para, F.; Cherioux, F.; Duverger, E.; Palmino, F.; Luzet, V.; Loppacher, C. Dipole-Driven Self-Organization of Zwitterionic Molecules on Alkali Halide Surfaces. *Beilstein J. Nanotechnol.* **2012**, *3*, 285–293.
22. Ostendorf, F.; Schmitz, C.; Hirth, S.; Kuhnle, A.; Kolodziej, J. J.; Reichling, M. Evidence for Potassium Carbonate Crystallites on Air-Cleaved Mica Surfaces. *Langmuir* **2009**, *25*, 10764–10767.
23. Negri, C.; Manini, N.; Vanossi, A.; Santoro, G. E.; Tosatti, E. AFM Dissipation Topography of Soliton Superstructures in Adsorbed Overlayers. *Phys. Rev. B* **2010**, *81*.
24. Synge, E. H. A Suggested Method for Extending Microscopic Resolution into the Ultra-Microscopic Region. *Philos. Mag.* **1928**, *6*, 356–362.
25. Betzig, E.; Trautman, J. K.; Harris, T. D.; Weiner, J. S.; Kostelak, R. L. Breaking the Diffraction Barrier-Optical Microscopy on a Nanometric Scale. *Science* **1991**, *251*, 1468–1470.
26. Novotny, L.; Sanchez, E. J.; Xie, X. S. Near-Field Optical Imaging Using Metal Tips Illuminated by Higher-Order Hermite-Gaussian Beams. *Ultramicroscopy* **1998**, *71*, 21–29.
27. Pohl, D. W.; Denk, W.; Lanz, M. Optical Stethoscopy-Image Recording with Resolution Lambda/20. *Appl. Phys. Lett.* **1984**, *44*, 651–653.

28. Vanhulst, N. F.; Moers, M. H. P.; Bolger, B. Near-Field Optical Microscopy in Transmission and Reflection Modes in Combination with Force Microscopy. *J. Microsc.* **1993**, *171*, 95–105.

29. Vanhulst, N. F.; Moers, M. H. P.; Noordman, O. F. J.; Tack, R. G.; Segerink, F. B.; Bolger, B. Near-Field Optical Microscope Using a Silicon-Nitride Probe. *Appl. Phys. Lett.* **1993**, *62*, 461–463.

30. Zenhausern, F.; Martin, Y.; Wickramasinghe, H. K. Scanning Interferometric Apertureless Microscopy-Optical Imaging at 10 Angstrom Resolution. *Science* **1995**, *269*, 1083–1085.

31. Zenhausern, F.; Oboyle, M. P.; Wickramasinghe, H. K. Apertureless Near-Field Optical Microscope. *Appl. Phys. Lett.* **1994**, *65*, 1623–1625.

32. Lulevich, V.; Ducker, W. A. Scanning Near-Field Optical Microscopy Utilizing Silicon Nitride Probe Photoluminescence. *Appl. Phys. Lett.* **2005**, 87.

33. Lulevich, V.; Honig, C.; Ducker, W. An Atomic Force Microscope Tip as a Light Source. *Rev. Sci. Instrum.* **2005**, 76.

34. Hulteen, J. C.; Vanduyne, R. P. Nanosphere Lithography-A Materials General Fabrication Process for Periodic Array Surfaces. *J. Vac. Sci. Technol., A* **1995**, *13*, 1553–1558.

35. Dimitrov, A. S.; Nagayama, K. Continuous Convective Assembling of Fine Particles into Two-Dimensional Arrays on Solid Surfaces. *Langmuir* **1996**, *12*, 1303–1311.

36. Kondo, M.; Shinozaki, K.; Bergstrom, L.; Mizutani, N. Preparation of Colloidal Monolayers of Alkoxylated Silica Particles at Air−Liquid Interface. *Langmuir* **1995**, *11*, 394–397.

37. Kralchevsky, P. A.; Denkov, N. D. Capillary Forces and Structuring in Layers of Colloid Particles. *Curr. Opin. Colloid Interface Sci.* **2001**, *6*, 383–401.

38. Mullen, T. J.; Zhang, M.; Feng, W.; El-khouri, R. J.; Sun, L. D.; Yan, C. H.; Patten, T. E.; Liu, G. Y. Fabrication and Characterization of Rare-Earth-Doped Nanostructures on Surfaces. *ACS Nano* **2011**, *5*, 6539–6545.

39. Haynes, C. L.; Van Duyne, R. P. Nanosphere Lithography: A Versatile Nanofabrication Tool for Studies of Size-Dependent Nanoparticle Optics. *J. Phys. Chem. B* **2001**, *105*, 5599–5611.

40. Yeshchenko, O. A.; Dmitruk, I. M.; Alexeenko, A. A.; Dmytruk, A. M. Size-Dependent Melting of Spherical Copper Nanoparticles Embedded in a Silica Matrix. *Phys. Rev. B* **2007**, 75.

41. Chan, G. H.; Zhao, J.; Hicks, E. M.; Schatz, G. C.; Van Duyne, R. P. Plasmonic Properties of Copper Nanoparticles Fabricated by Nanosphere Lithography. *Nano Lett.* **2007**, *7*, 1947–1952.

42. Bakker, R. M.; Drachev, V. P.; Yuan, H. K.; Shalaev, V. M. Near-Field, Broadband Optical Spectroscopy of Metamaterials. *Physica B* **2007**, *394*, 137–140.

43. Des Francs, G. C.; Girard, C.; Bruyant, A.; Dereux, A. SNOM Signal Near Plasmonic Nanostructures: An Analogy with Fluorescence Decays Channels. *J. Microsc.* **2008**, *229*, 302–306.

44. Foteinopoulou, S.; Vigneron, J. P.; Vandenbem, C. Optical Near-Field Excitations on Plasmonic Nanoparticle-Based Structures. *Opt. Express* **2007**, *15*, 4253–4267.

45. Lee, Y.; Alu, A.; Zhang, J. X. J. Efficient Apertureless Scanning Probes Using Patterned Plasmonic Surfaces. *Opt. Express* **2011**, *19*, 25990–25999.

46. Lin, H. Y.; Huang, C. H.; Chang, C. H.; Lan, Y. C.; Chui, H. C. Direct Near-Field Optical Imaging of Plasmonic Resonances in Metal Nanoparticle Pairs. *Opt. Express* **2010**, *18*, 165–172.

47. Wurtz, G. A.; Im, J. S.; Gray, S. K.; Wiederrecht, G. P. Optical Scattering from Isolated Metal Nanoparticles and Arrays. *J. Phys. Chem. B* **2003**, *107*, 14191–14198.

48. Chen, Z. G.; Xu, Z. P.; Zhang, M.; Zhou, Y.; Liu, M.; Patten, T.; Liu, G. Y.; Li, H.; Zeng, X. C.; Tan, L. Two-Dimensional Crystallization of Hexagonal Bilayer with Moiré Patterns. *J. Phys. Chem. B* **2012**, *116*, 4363–4369.

49. Li, J. R.; Henry, G. C.; Garno, J. C. Fabrication of Nanopatterned Films of Bovine Serum Albumin and Staphylococcal Protein A Using Latex Particle Lithography. *Analyst* **2006**, *131*, 244–250.

50. Li, J.-R.; Yin, N.-N.; Liu, G.-Y. Hierarchical Micro- and Nanoscale Structures on Surfaces Produced Using a One-Step Pattern Transfer Process. *J. Phys. Chem. Lett.* **2011**, *2*, 289–294.

51. Hulteen, J. C.; Treichel, D. A.; Smith, M. T.; Duval, M. L.; Jensen, T. R.; Van Duyne, R. P. Nanosphere Lithography: Size-Tunable Silver Nanoparticle and Surface Cluster Arrays. *J. Phys. Chem. B* **1999**, *103*, 3854–3863.

52. Li, J. R.; Garno, J. C. Elucidating the Role of Surface Hydrolysis in Preparing Organosilane Nanostructures *via* Particle Lithography. *Nano Lett.* **2008**, *8*, 1916–1922.